# III. Experimental Setup

## A. Beam-line Arrangement

The beam-line begins with the **CRY**ogenic **E**lectron **B**eam **I**on **S**ource (**CRYEBIS**) **[3.1, 3.2]**, where the ions to be used as projectiles are made. The ions are extracted from the **CRYEBIS**, and mass/charge selected using an analyzing magnet, which directs the projectile ions into the **O**cta-**P**ole **I**on beam **G**uide (**OPIG**) apparatus. A 10 cm length gas cell inside the **OPIG** is used to contain the target gas, and is the region where the low energy collisions occur. As the ions exit the **OPIG**, they are re-focused, and pass a second charge state analyzing magnet, which is used to separate the primary beam from the single and double capture beams. After passing through this analyzing magnet, the ions are directed onto a position sensitive ion detector.

There are two main features of an **OPIG** that make it possible to measure very low energy electron capture cross sections. First, the **OPIG** decelerates the ion beam. Secondly, the **OPIG** acts as a trap in the transverse direction. The entire **OPIG** system can be floated with a positive electric potential, and tuning this potential tunes the collision energy, where the collision energy is defined as the difference in the extraction voltage of the **CRYEBIS** and the potential on the **OPIG** multiplied by the charge of the ion. The **OPIG** also incorporates the use of a radio-frequency (*r-f*) voltage that is applied to the eight wires which constitute the octapole. These wires have the geometric configuration which inscribes a circle with the ion beam axis at the center. The *r-f* voltage, applied to the wires in this configuration, generates a field that confines the ions in the direction transverse to the ion beam axis.

Upon exiting the **OPIG**, the re-accelerated ions pass a three element electrostatic lens, a pair of quadrupole lenses, and a horizontal and vertical steerer, which are used to refocus the beam. Since the projectile ions may have captured one or more electrons from the atoms of the gas target, and it is wished to measure the probability of this capture process, it is necessary to separate out the different ion species after they have passed through the collision region. Two methods have been employed to separate the primary ion beam from the single and double electron-captured ions. The first method discussed is referred to as the retarding grid technique. The second method for separation is referred to as the magnetic charge state analyzing technique. The retarding plate technique was used in the initial stages of the experiment, and some data was acquired in this way. However, the magnetic charge state analyzing technique was used to acquire the major portion of the data because the separation of the different charge states depends on the charge to mass ratio of the ions, whereas, the separation of the different charge states using the retarding grid technique depends on both the energy and charge of the ions, and ultimately has a poorer resolution.

## 1. Retarding Grid Technique

This technique involves the use of an ion retardation detector system. Four meshed electrodes are positioned directly downstream from the **OPIG**, and are used to separate the primary ion beam from the projectile ions that have captured electrons. All ions that pass through the retardation grids, are measured on a beam viewer, which consists of two micro-channel plates in the chevron arrangement, followed by a phosphor screen. The phosphor screen will then fluoresce whenever an ion strikes the channel

plates. A mirror is situated behind the phosphorus screen, so that this fluorescence can be monitored with a CCD camera, positioned above the beam line.

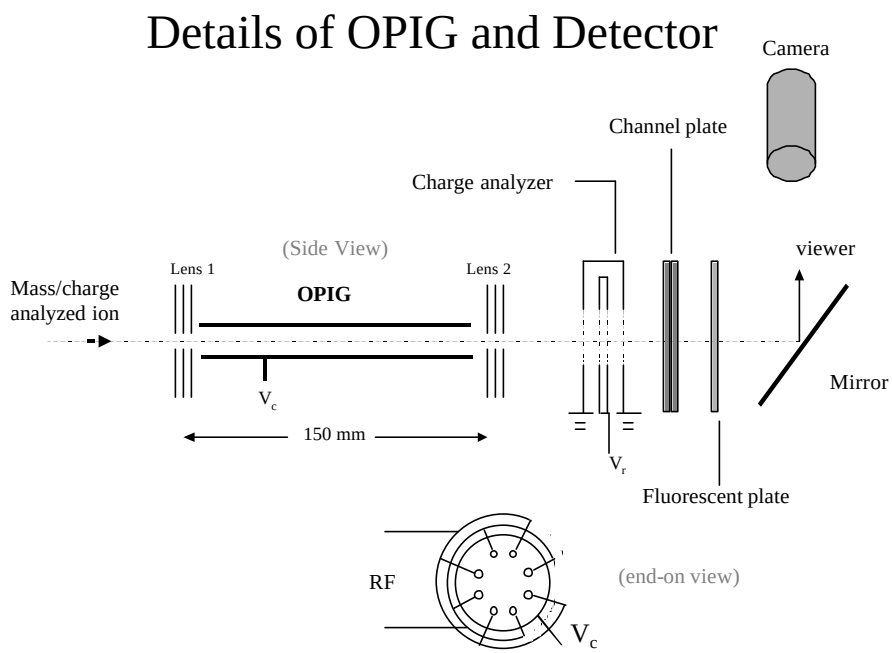


**Figure 3.1** **OPIG** and beam-line arrangement, using a set of retarding meshes to separate different charge species product ions after passing through the target chamber.

The initial energy of the ion beam, $E_i$, extracted from the **CRYEBIS** can be expressed as, $E_i = q*V_E$ where $q$ is the charge of the ion, and $V_E$ is the extraction voltage of the **CRYEBIS**. The energy the ion has upon entering the **OPIG** is $E= q(V_E - V_C)$, where $V_C$ is the electric potential of the **OPIG**. While inside the **OPIG** the projectile may have captured one or two electrons. The energy of the of the primary, single capture, and double capture beams, will be; $E_P = E_i$, $E_S = q(V_E - V_C) + q'(V_C)$, and $E_D = q(V_E - V_C) + q''(V_C)$, where $E_P$ is the energy of the primary ions, $E_S$ is the energy

of the single capture ions, and $E_D$ is the energy of the double capture ions. Also, $q' = (q-1)$ and $q'' = (q-2)$. Now, $V_{RP}$, $V_{RS}$, and $V_{RD}$, are the voltages required to stop the primary ions, single capture ions, and double capture ions respectively, and can be expressed as;

$$V_{RP} = V_E, \qquad \textbf{(Eq. 3.1)}$$

$$V_{RS} = (q/q')(V_E - V_C) + V_C \qquad \textbf{(Eq. 3.2)}$$

and

$$V_{RD} = (q/q'')(V_E - V_C) + V_C. \qquad \textbf{(Eq. 3.3)}$$

All ions will pass the retarding meshes for voltages when $V_R < V_{RP}$, where $V_R$ is the voltage of the retarding meshes. For $V_{RP} < V_R < V_{RS}$, the primary ions will not pass the retarding meshes, but the single and double capture ions will still be able to pass. For $V_{RS} < V_R < V_{RD}$, only the double capture ions will be able to pass the retarding plates. Data are accumulated by recording a count rate with $V_R$ set to a voltage in each of these three different regimes. These count rates are then used to calculate the cross sections for single and double electron capture, as described below.

While the use of retarding meshes to separate primary ions from those of single and double capture was an acceptable method to measure capture cross sections, it was abandoned in favor of the use of a charge state analyzing magnet. The use of a charge state analyzing magnet allowed for a greater range of projectile ion species and charge states to be used for cross section measurements at very low energies due to the improved energy resolution this method offered. However, the retarding mesh system did produce valuable results, and are summarized in **[3.3]**.

## 2. Charge State Analyzing Magnet Technique

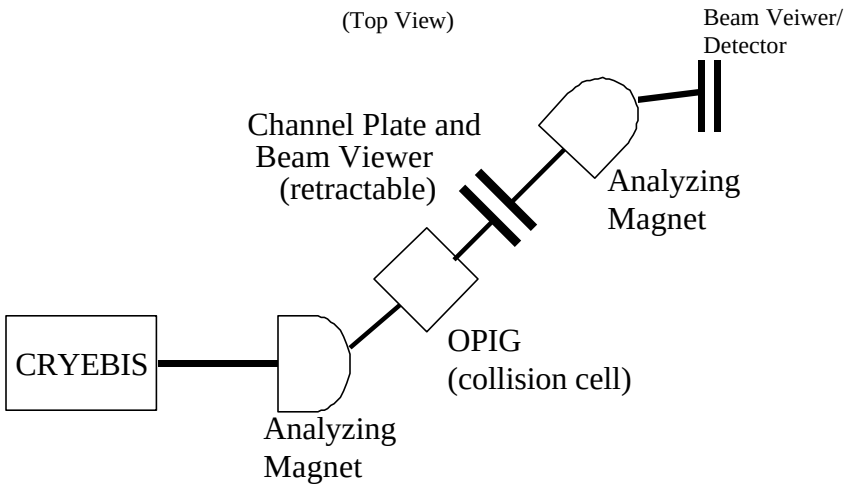


**Figure 3.2** **OPIG** and beam-line arrangement, using a charge-state analyzing magnet to separate different charge species product ions after passing through the target chamber. A position sensitive detector is used to measure the product ions.

Using the second technique, separating the different ion charge states is accomplished with the use of a charge-state analyzing magnet. Each ion is deflected by an angle that is proportional to its charge. With proper tuning, the ion charge states can be separated and viewed on a retractable beam viewer, located downstream from the charge-state analyzing magnet. The beam viewer is about 5 cm in front of the detector, and is used to visually confirm that the ions are properly separated and focused. Once the focusing is optimized, the beam viewer is removed from the ion beam path, and the ions can then be detected on a standard wedge-and-strip backgammon position sensitive detector **[3.4]**.

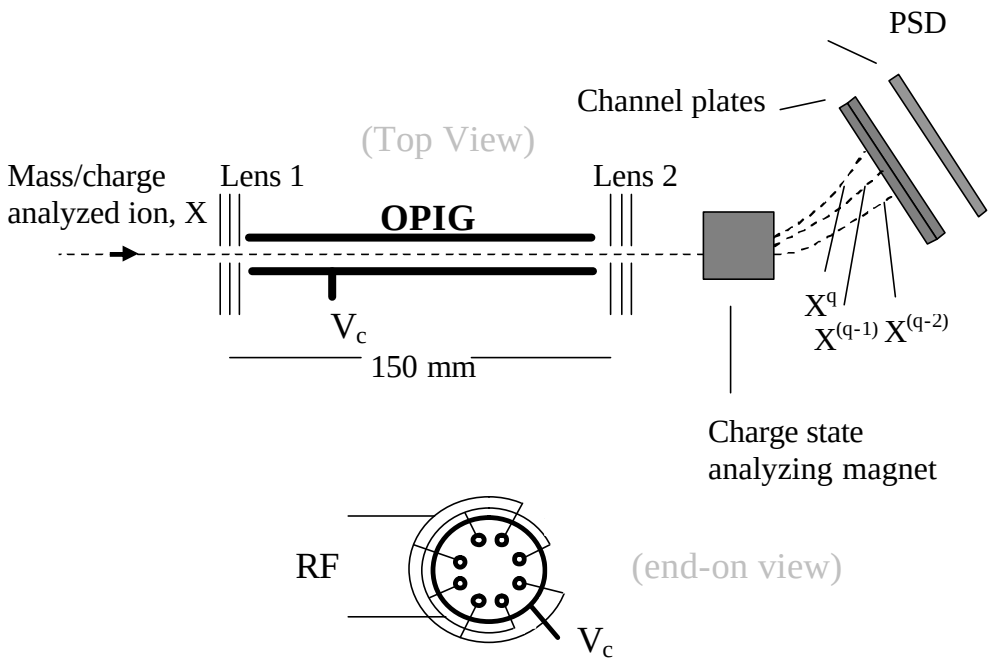


**Figure 3.3** Side and end-on view of the **OPIG**, with the charge-state analyzing magnet and position sensitive detector.

Typically, it was necessary to measure the primary beam, and the single capture beam in one run, and then take a second run, measuring only the single and double capture beams. Since the primary beam was much more intense than the single and double capture beams, more beam attenuation was needed for runs where the primary and single capture beam was measured, than for the run where the single and double capture beams were measured. The ratio of the double capture count rate to single capture count rate was determined from the second run, where the single capture and double capture beams were measured. This ratio was then multiplied by the single capture count rate from the first run, to generate what the double capture count rate would have been in the

first run. The magnetic field is adjusted between runs so as to center the primary beam and single capture beam for one run, and the single capture and double capture beams in the following run. In this manner, the count rates for the primary beam, single electron capture beam, and double electron capture beam can all be measured, and compared on equal footing.

## B. Production of Projectile Ions from the **CRYEBIS**

As stated above, the projectile ions used in this experiment are created in the **CRYEBIS**. For this experiment, the ions are extracted with an initial energy of 3kV(q) before the 90-degree analyzing magnet of the **CRYEBIS**. The desired charge state is selected using this 90-degree analyzing magnet. The entire **CRYEBIS** is floated on a potential of 1 kV. The energy of the ions, as they exit the **CRYEBIS** cage is 2 kV(q). The **CRYEBIS** preferentially produces ions in the ground state **[3.5]**, which is helpful in simplifying the net electron capture cross section analysis, since the electron capture cross sections may strongly depend on the initial state of the primary ions at low collision energies. Ions extracted from the **CRYEBIS** are almost exclusively in the ground state because the confinement time of the ions is long enough that any excited states created decay before extraction. Also, the ion source neutral gas pressure is kept very low, so that electron capture inside the ion source is inhibited, thereby making the creation of excited state ions unlikely.

## C. The Octapole Ion Beam Guide

The **OPIG** operates in a manner similar to a tandem mass spectrometer. One difference is that an **OPIG** is combined with a collision cell, and used to avoid divergence of several different charge/mass ratio ions (i.e. the primary beam, and single and double electron capture beams), instead of selecting a particular ion charge/mass ratio to be guided through the apparatus. An ion beam from the **CRYEBIS** is directed through a switching magnet to the proper beam line (beam-line A), where the ions enter the **OPIG**, and may undergo a collision with an atom in the gas target.

### 1. Design

The **OPIG** system used in this experiment was designed and built by Professor K. Okuno, at Tokyo Metropolitan University (TMU), in Minami-Osawa, Tokyo. The **OPIG** used in this experiment is a slightly modified reconstruction of the same device used by Professor Okuno at TMU **[3.6, 3.7, 3.8, 3.9]**.

#### a. Deceleration

As stated previously, a positive potential is applied to the entire **OPIG** system. The amplitude of this potential determines the collision energy. Generally, when an ion beam is decelerated, the beam spreads out in the transverse direction to the ion beam axis, but by using an **OPIG** to decelerate the ion beam, the ions are confined due to the r-f field applied to the octapole, which acts as a trap in the transverse direction. In order to keep the beam focusing optimized, apertures are used as electrostatic lenses on the entrance and exit of the **OPIG**. The first aperture on the entrance side of the **OPIG** is

0.85mm in diameter, and the following apertures are 1mm in diameter. There are a total of three entrance electrodes on the upstream side of the **OPIG**. The first electrode is used monitor the intensity of the primary ion beam. By adjusting their potentials, the second and third entrance electrodes are used to optimize the focusing of the ion beam as it enters the **OPIG**. The three aperatures on the downstream side of the **OPIG** are used to refocus the ion beam after as it is re-accelerated upon exiting the **OPIG**.

### b. RF Voltage, and Transverse Confinement of The Ion Beam - Impedance Matching Interface Circuit

Eight molybdenum rods, 1.5 mm in diameter, and 15cm in length, which are equally spaced, and inscribe a 7 mm cylinder, with the ion beam on the axis of the cylinder. An *r-f* generator (Hewlett Packard, 8654A, 10-250 MHz) signal is sent into an amplifier (ENI 32000L, 55 dB, 250 kHz – 150 MHz), and the output of the amplifier is sent into an impedance matching interface circuit. The r-f electric field in the **OPIG** is operated at a frequency of 16 MHz, and has an amplitude of approximately 300 volts. This field is used to keep the ion beam from spreading in the transverse direction to the ion beam axis, while the ion beam is passing through the **OPIG** with very low energy. The impedance matching unit is essentially an LC circuit, where the octapole itself provides most of the capacitance in the circuit. The entire octapole is floated on the electric potential, $V_c$. The circuit is designed so that alternating wires of the octapole are at the same potential.

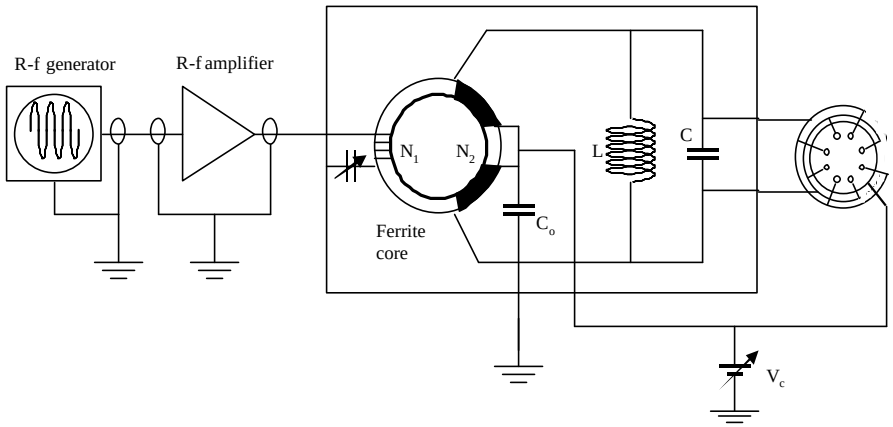


**Figure 3.4** Schematic diagram of the impedance matching circuit. The output of this device goes to the eight wires of the octapole, providing the field that confines the projectile ions in the tranverse direction to the ion beam axis.

The two sets of 4 wires have an equal potential magnitude, but opposite polarity. By attaching probes to the signals that are delivered to each set of 4 wires, the signals can be monitored on an oscilloscope. When the circuit is at the resonant frequency, the power is optimally transmitted to the octapole, and this resonance can be observed by comparing the two signals. The signals of the two sets of 4 wires will be 180 degrees out of phase, and equal in magnitude, and will reach a maximum amplitude when at the resonant frequency.

## 2. The Physical Principles and Performance of An **OPIG**

### a. Transverse Trapping Potential in an **OPIG**

The potential around the central axis of a $2N$ multi-pole beam guide ($2N = 8$ for an octapole), where the poles are equally spaced around the axis, and have oscillatory voltages of $\pm V_{rf} \cos(wt)$ applied to them alternatively in opposite phases, is

$$U = \left(\frac{r}{a}\right)^N V_{rf} \cos(Nq)\cos(wt)\,, \qquad \textbf{(Eq. 3.4)}$$

where $r$ and $q$ are the position in cylindrical coordinates, $a$ is the close radius of the inscribed circle of the poles, $t$ is the time, $V_{rf}$ is the amplitude of the *r-f* voltage with a frequency of $w/(2\pi)$. This oscillatory electric field modulates the motion of charged particles in the radial direction, but does not change the translational kinetic energy of the charged particles along the axis of the **OPIG**.

The trajectory of a charged particle in a multi-pole beam guide (with $N \geq 2$) projected on the x-y plane (perpendicular to the **OPIG** axis) can be obtained from the following differential equations.

$$\frac{d^2x}{dt^2} = -\frac{Nq}{ma}\left(\frac{x}{a}\right)^{N-1} V_{rf} F_N \cos(wt)\,, \qquad \textbf{(Eq. 3.5)}$$

$$\frac{d^2y}{dt^2} = \frac{Nq}{ma}\left(\frac{y}{a}\right)^{N-1} V_{rf} G_N \cos(wt)\,, \qquad \textbf{(Eq. 3.6)}$$

where $m$ and $q$ are the mass and charge of the particle. $F_N$ and $G_N$ are represented by

$$F_N = \frac{\cos[(N-1)q]}{(\cos q)^{N-1}} = \sum_{j=0}^{[(N-1)/2]} (-1)^j \begin{bmatrix} N-1 \\ 2j \end{bmatrix} \left(\frac{y}{x}\right)^{2j}, \qquad \textbf{(Eq. 3.7)}$$

and

$$G_N = \frac{\sin[(N-1)q]}{(\sin q)^{N-1}} = \sum_{j=0}^{[(N-2)/2]} (-1)^j \begin{bmatrix} N-1 \\ 2j+1 \end{bmatrix} \left(\frac{x}{y}\right)^{N-2j-2}. \qquad \textbf{(Eq. 3.8)}$$

For N=2, these equations are analytically the same as the Mathiew equations for the ion motion in a quadrupole mass filter when the electrostatic voltage vanishes. In the operation of a mass filter, it can be observed that much greater ion transmission can be achieved at the expense of mass resolution when the electrostatic potential is lowered. This fact helps in understanding why the oscillatory electric field of the **OPIG** is so effective in guiding charged particles.

To simulate the trajectory of various charged particles, at several different collision energies, a direct stepwise-integration of **Equation 3.5** and **Equation 3.6** has been evaluated using Microsoft Excel, a spreadsheet program. The x-y projection of a charged particle trajectory is shown in **Figure 3.5**, for $Ar^{+8}$ with an axial velocity, $V_z$ = $6.9 \times 10^5$ cm/sec.

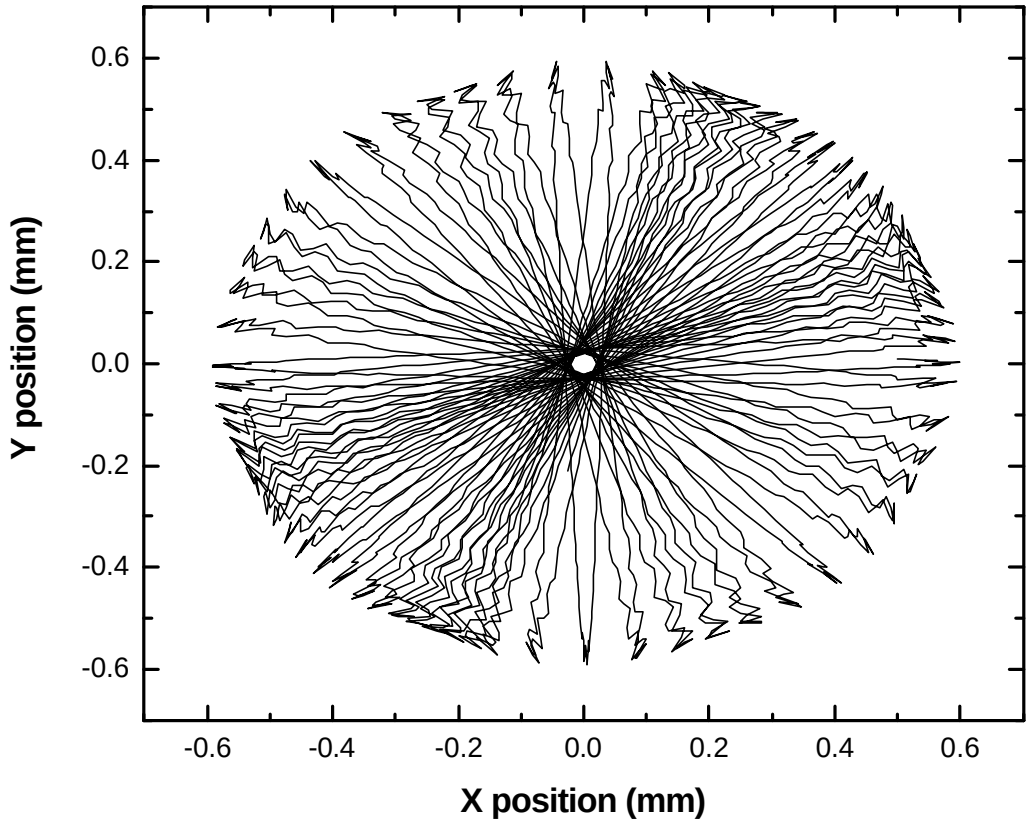


**Figure 3.5** A plot displaying the x-y projection of an $Ar^{+8}$ ion as it passes through the **OPIG**, generated by doing a stepwise integration of **Equation 3.5** and **Equation 3.6**. The ions motion is determined by its velocity entering the **OPIG**, and the radio-frequency electric field of the octapole. Initial conditions are $x_0 = 0.05$, $y_0 = 0$ cm for the injecting point, $V_x = 1.2$, $V_y = 0.6$, $V_z = 6.9 \times 10^5$ cm/sec for velocity.

Using $N > 2$, the scaling

$$T = wt \qquad \text{and} \qquad R = \left(\frac{r}{a}\right)\left(\frac{NqV_{rf}}{m(aw)^2}\right)^{1/(N-2)}, \qquad \textbf{(Eq. 3.9)}$$

can be used to express **Equation 3.5** and **Equation 3.6** in cylindrical coordinates as

$$\frac{d^2R}{dT^2} - R\left(\frac{dq}{dT}\right)^2 = -R^{(N-1)}\cos(Nq)\cos(T)\,, \qquad \textbf{(Eq. 3.10)}$$

and

$$2\frac{dR}{dT} + R\frac{d^2q}{dT^2} = R^{(N-1)}\sin(Nq)\cos(T)\,, \qquad \textbf{(Eq. 3.11)}$$

which simplifies the analytical treatment of the ion motion in a multi-pole beam guide. Using this scaling, the ion motion can be separated into two terms. One term describes the fast oscillatory motion of the ion, and the other describes an average motion of the ion. These are

$$R(T) = R_{av}(T) + R_{os}(R_{av}, q_{av}; T) \qquad \textbf{(Eq. 3.12)}$$

and

$$q(T) = q_{av}(T) + q_{os}(R_{av}, q_{av}; T)\,. \qquad \textbf{(Eq. 3.13)}$$

When the frequency of the *r-f* field is large enough, the terms describing the average position (which describes the "slowly-changing" motion) of the ion will change very little during time intervals where $wt = 2\pi$. The oscillatory terms can be approximated as

$$R_{os} = R_{av}^{(N-1)}\cos(Nq_{av})\cos(T) \qquad \textbf{(Eq. 3.14)}$$

and

$$q_{os} = -R_{av}^{(N-2)}\sin(Nq_{av})\cos(T)\,. \qquad \textbf{(Eq. 3.15)}$$

These oscillatory terms, $R_{os}$ and $q_{os}$, become nearly negligible when the frequency is great enough, and the average trajectory (when $|R_{av}| << 1$) of the ion can be approximated by the average motion, which can be derived from the following relations

$$\frac{1}{2}\left(\frac{dR_{av}}{dT}\right)^2 + \frac{1}{2}\left(\frac{M}{R_{av}}\right)^2 + \frac{1}{4}(R_{av})^{2(N-1)} = E_{T=0} \qquad \textbf{(Eq. 3.16)}$$

and

$$(R_{av})^2 \frac{dq_{av}}{dT} = M_{T=0}, \qquad \textbf{(Eq. 3.17)}$$

where $E_{T=0}$ and $M_{T=0}$ are the initial components of the energy and angular momentum of the ion beam, upon entering the **OPIG**, and these quantities are conserved throughout the length of the **OPIG**. The ion trajectory, as given by this approximation, is ordinary periodic motion due to a conserving force arising from an effective potential of

$$U_{eff} = \frac{(NqV_{rf})^2}{4m(aw)^2}\left(\frac{r}{a}\right)^{2(N-1)}. \qquad \textbf{(Eq. 3.18)}$$

Furthermore, the average trajectory is close to the exact one. Since the number of poles, 2*N*, is in the exponent of the expression for the effective potential, the number of poles greatly influences the strength of the reflective potential wall, or ability for the multi-pole to confine ions in the transverse direction. Also, the field-free region around the central axis is increased, as the number of poles is incremented.

To confine an ion with an energy $E_m$ in the guide one has to satisfy the following stability criteria for the minimum *r-f* voltage $V_{min}$ and minimum frequency $\omega_{min}$ on the octapole [**3.10**]

$$V_{\min} = 8\frac{N-1}{N}\frac{E_m}{qh_m r_m^N}, \qquad \textbf{(Eq. 3.19)}$$

and

$$w_{\min} = \frac{1}{2p}\sqrt{\frac{16(N-1)^2 E_m}{m(h_m r_0 r_m)^2}}. \qquad \textbf{(Eq. 3.20)}$$

## b. Kinematics Involved in Slow Electron-Capture Collisions

In highly charged ion collisions, the charge transfer process is exoergic resulting in the release of energy, Q, which can result in the ions being scattered. Without the use on an **OPIG**, this scattering would reduce the collection efficiency for the ions, especially for low energy collisions. However, in collisions where the mass of the projectile is much larger than that of the targets, the product ions will be scattered in the forward direction in the laboratory system. Therefore, in this experiment, nearly all product ions can be detected in the whole collision energy range.

The velocity vector diagram of **Figure 3.6** illustrates the kinematics involved in an inelastic collision between a projectile ion $A^{q+}$ that has a mass of $m_a$ and velocity $v_o$, and an atom B with a mass $m_b$, that is at rest in the lab frame. When the projectile ion undergoes this inelastic capture process (it is then referred to as the product ion $A^{(q-r)+}$), it is scattered into an angle $T_a$ with a velocity $v_a$ in the laboratory frame. After the collision, the recoil ion $B^{r+}$, will scatter into an angle $T_b$ with a velocity $v_b$ in the laboratory frame. In center-of-mass coordinates, the center-of-mass of the product ion and the recoil ion is scattered through an angle T. Since the collision is exoergic, the total kinetic energy after the collision, $E_{rf} = (1/2)\mu v_r^2$, is greater than the total kinetic energy before the collision, $E_{ri} = (1/2)\mu v_o^2$, by the energy gain Q. Here, $E_{rf}$ is the kinetic energy after the collision, $E_{ri}$ is the kinetic energy before the collision, μ is the reduced mass, and $v_r$ is the relative velocity after the collision, and $Q = E_{rf} - E_{ri}$. From **Figure 3.6**, the component of the scattered ion velocity that lies along the original ion beam direction in the laboratory system is related to the angle T in the center-of-mass system by

$$v_a \cos q_a = v_g\{1 + (m/m_a)(v_r/v_g)\cos\Theta\} \qquad \textbf{(Eq. 3.21)}$$

and

$$v_b \cos q_b = v_g\{1-(m/m_b)(v_r/v_g)\cos\Theta\} \qquad \textbf{(Eq. 3.22)}$$

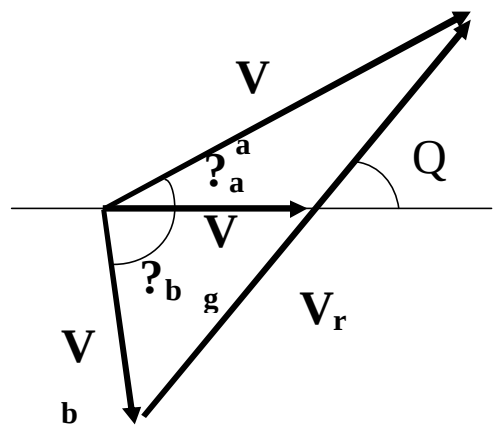


**Figure 3.6** Velocity vector diagram of an inelastic collision between a projectile ion $A^{q+}$ and an atom B, in the center-of-mass coordinates.

Then from **Equation 3.21** and **Equation 3.22**, it is found that $A^{(q-r)+}$ and $B^{r+}$ ions with positive axial velocity components ($\theta_a < \pi/2$ and $\theta_b < \pi/2$) will be distributed in the angular regions of $0 \le \Theta < \Theta_a$ and $\Theta_b < \Theta \le \pi$, in the center-of-mass frame, respectively. The measurable angle limits for $\Theta_a$ at $\theta_a = \pi/2$ and $\Theta_b$ at $\theta_b = \pi/2$ are given from the relations

$$1+(m_b/m_a)(Q/E_{r0}+1)^{1/2}\cos\Theta_a = 0 \qquad \textbf{(Eq. 3.23)}$$

and

$$1-(Q/E_{r0}+1)^{1/2}\cos\Theta_b = 0\,. \qquad \textbf{(Eq. 3.24)}$$

In **Figure 3.7**, the angular limit for $T_a$ is shown as a function of $E_{r0}/Q$, where the measurable T for $A^{(q-r)+}$ is below the $T_a$ curves (1) - (5), which illustrates the effect that the projectile ion to target mass ratio has on collection efficiency. For the case in which $m_a >> m_b$, essentially all product ions, for a wide range of energies, will be guided along the ion beam axis with the use of an **OPIG**. Even at very low values of $E_{r0}/Q$, almost all ions will be guided through the **OPIG**. However, when the projectile ion to target mass ratio is very small, $m_a << m_b$ the ions that can be measured is limited to those scattered into $0 \leq \Theta < \Theta_a$.

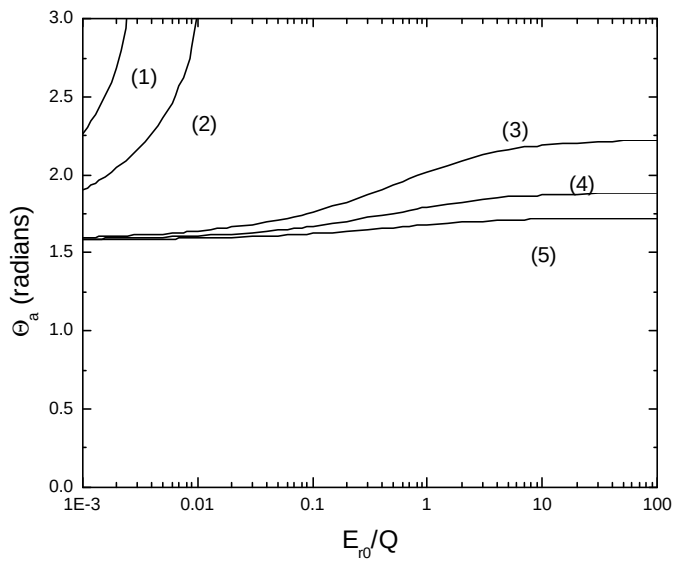


**Figure 3.7** The **OPIG**'s measurable angle limits, $\Theta_a$ as a function of $E_{r0}/Q$. The curves, (1), (2), (3), (4), and (5) are the upper limits of the angle, $\Theta_a$, that projectile ions can be detected using the **OPIG** for collision systems with $m_a/m_b$ = 40/2, 40/4, 12/20,12/40, and 12/84 respectively.

## D. Ion Beam and Target Preparation with Magnetic Separation

### 1. Tuning, and Focusing

After the ions are guided through the **OPIG**, and re-accelerated, focusing can be achieved by using the electrode lens system attached to the downstream end of the **OPIG**, as previously described. Additional focusing is achieved with the use of a pair of static quadrupole lenses, a vertical steerer, and a horizontal steerer, which are mounted just after the downstream end electrodes of the **OPIG**.

A diagram illustrating the configuration of the ion beam focusing elements on the downstream end of the **OPIG** is shown in **Figure 3.8**.

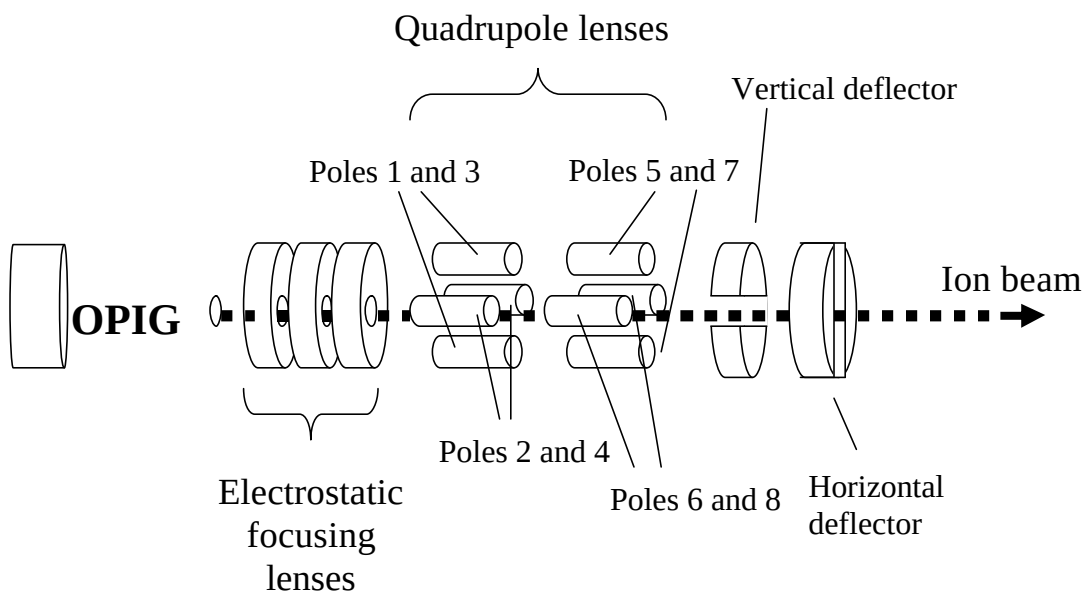


**Figure 3.8** A 3-dimensional view of the arrangement of the two sets of quadrupole lenses, and the vertical and horizontal steerer on the downstream end of the **OPIG** (analyzing magnet and detector not shown).

The quadrupole elements are paired, where each pair is set at the same electric potential. For convenience in describing the apparatus, a numbering scheme is used to label the poles. The poles are in pairs, 1-3, 2-4, 5-7, and 6-8, where each pair has a common electric potential. With the 1-3 pair set to a negative voltage, the 2-4 pair is at a positive voltage. Pair 5-7 is positive, and 6-8 is negative. The voltage settings for each pair will vary from one experiment to the next, and depends on the ion beam charge and mass to some degree, as well as the particular orientation with which the beam is injected into the **OPIG.** (A SIMION program has been used to simulate the effect of the quadrupoles and vertical and horizontal steerers. More details about this program can be found in **Appendix 1**).

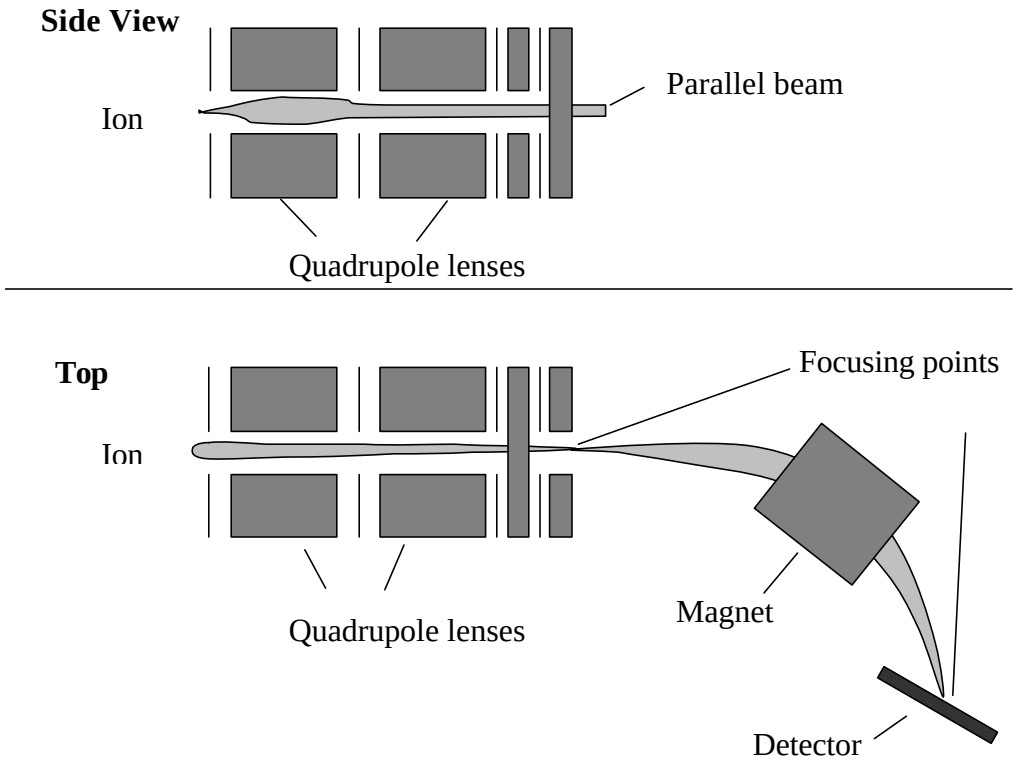


**Figure 3.9** Side and top views of the quadrupole lenses attached to the downstream end of the **OPIG** to illustrate the ion beam focusing.

The quadrupole arrangement is designed to focus on both the vertical and horizontal axis. As can be seen from the side view in **Figure 3.9**, the effect of the first quadrupole is to broaden the ion beam in the vertical direction and squeeze it in the horizontal direction. The second quadrupole lens squeezes the ion beam enough to make it parallel in the vertical axis. The first and second quadrupoles are used to focus the ion beam before the analyzing magnet because the analyzing magnet acts as a lens in the horizontal direction. In this experiment, the focusing strength of the analyzing magnet was not exactly known, so the beam was simply monitored on the beam viewer, while the focusing was optimized. The rigidity of different charge states is nearly equal for ions of the same species, so this focusing technique works for each charge state. Ions with a greater charge will be deflected to a greater angle, but the focusing effect will be the same for all charge states of the same ion species.

## 2. Separation of Charge States, and Ion Detection

After passing through the **OPIG**, the ions then go through a charge state analyzing magnet, which is used to separate the single and double capture ions from the primary ion beam. The three separated beams can then be directed onto the beam viewer, which consists of two channel plates that are positioned in the standard chevron arrangement, and a phosphor screen, which is about 1cm behind the channel plates. The front channel plate is at ground potential with respect to the beam line, and the back channel plate is set at 2000 volts. The phosphor screen is usually set at a voltage of 5000 volts. The applied voltage on the phosphor screen is related to the relative energy of the ions incident on the channel plates. A smaller voltage is used for a larger current on the

channel plates. The phosphor screen will fluoresce when ions are incident on it, and this fluorescence is reflected by a mirror in place behind the phosphorus screen into a CCD camera and can be viewed on a monitor. The beam viewer provides a convenient way to visually observe that the beam is focused. With proper tuning and focusing of the ion beam, the different charge states can be clearly separated and individually focused. **Figure 3.10** demonstrates how the beam spots are focused onto the beam viewer under normal conditions.

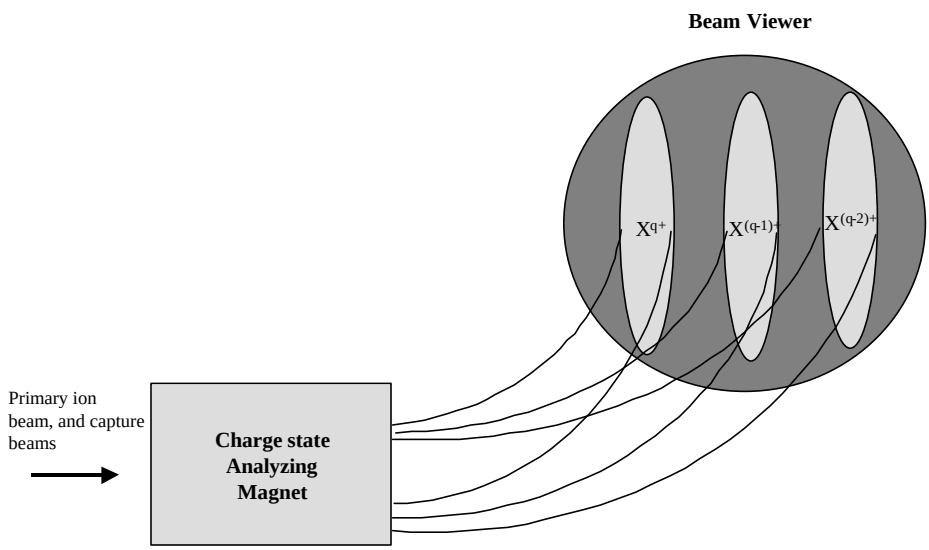


**Figure 3.10** A diagram illustrating how the primary beam, $X^{q+}$, and single and double capture beams, $X^{(q-1)+}$, and $X^{(q-2)+}$ are focused onto the beam viewer.

When performing an experiment, it can be seen visually that all three charge-states are hitting the beam viewer simultaneously.

## 3. Setting Target Pressure (Avoiding Double Collisions)

The entire system is maintained under vacuum, to ensure that the projectile ions will not interact with other atoms or molecules that would otherwise be present. The helium, hydrogen, argon, and neon gas targets used were 99.9% pure. Since the **OPIG** has small entrance and exit apertures, pumping is needed on both the upstream and downstream sides of the **OPIG**, as well as in the **OPIG** itself. Three turbo pumps are used, one for each of these respective segments of the beam-line. The upstream pressure is in the high $10^{-9}$ Torr range. The pressure inside the **OPIG** is in the low $10^{-5}$ Torr range, and the pressure on the downstream side of the **OPIG** is in the $10^{-7}$ Torr range. The length of the **OPIG** is 15 cm. The entire 15 cm length of the **OPIG** is set to a voltage for the desired collision velocity, and the r-f field applied to the octapole is floated on this voltage. The gas cell is 10 cm long, centered in the middle of the **OPIG** (2.5 cm to the upstream and downstream ends of the **OPIG**), and has 1mm apertures on its entrance and exit ends. The upstream and downstream sections adjacent to the **OPIG** are differentially pumped. The region outside of the gas cell, near the entrance and exit apertures will have a pressure that is higher than the average pressure of the upstream and downstream sections. As a rule of thumb, the pressure in the region outside the gas cell is believed to drop close to a background level at a distance about 1-3 radius (1mm) away from the gas cell on each side of the cell aperture. When performing cross section calculations, the value used for the length of the gas cell, *L*, was taken to be 10.5 cm.

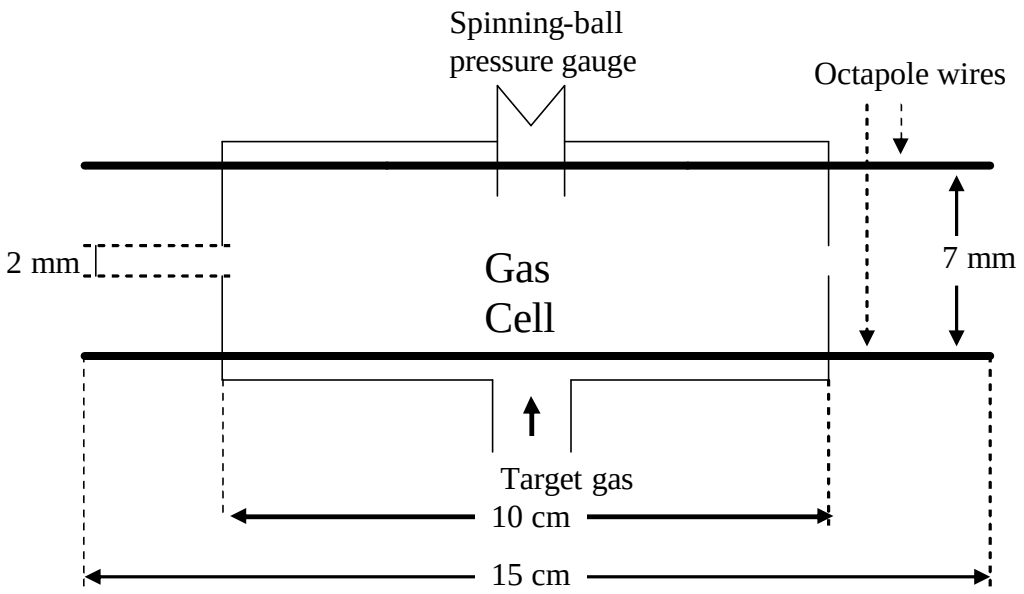


**Figure 3.11** Cross-sectional view of the **OPIG** and gas cell (not to scale).

In order to determine the best gas pressure, and ensure that double collisions are minimal, the target gas pressure was varied, with the **OPIG** voltages all set to zero. The ratio of single capture counts to the total counts, and the double capture counts to the total counts was measured. Testing the dependence of the double collisions on target pressure was done before the installation of the PSD. The beam viewer was modified so that the signal from the back channel plate of the beam viewer was input to a VT 120 pre-amplifier, and the output of the pre-amplifier went to a EG&G model AN201/N quad amplifier. The output of the amplifier was passed through an inverter, and input to a multi-scaler, which was used for counting.

Before performing pressure dependency tests, a measurement was made in which, as the ion beam current was varied the number of counts was recorded. This was done to ensure that the electronics used in the beam-counting system would not saturate

for the count rates in the pressure dependency tests. An $Ar^{+8}$ ion beam was used in this test, and the beam current was varied using a set of calibrated ion beam attenuators which are located upstream of the switching magnet. Three different attenuators were used, that pass 21%, 10%, and 1% of the **CRYEBIS** ion beam. This allowed for total ion beam fractions of 21%, 10%, 2.1%, 1%, 0.21%, and 0.1%. **Figure 3.12** shows the count

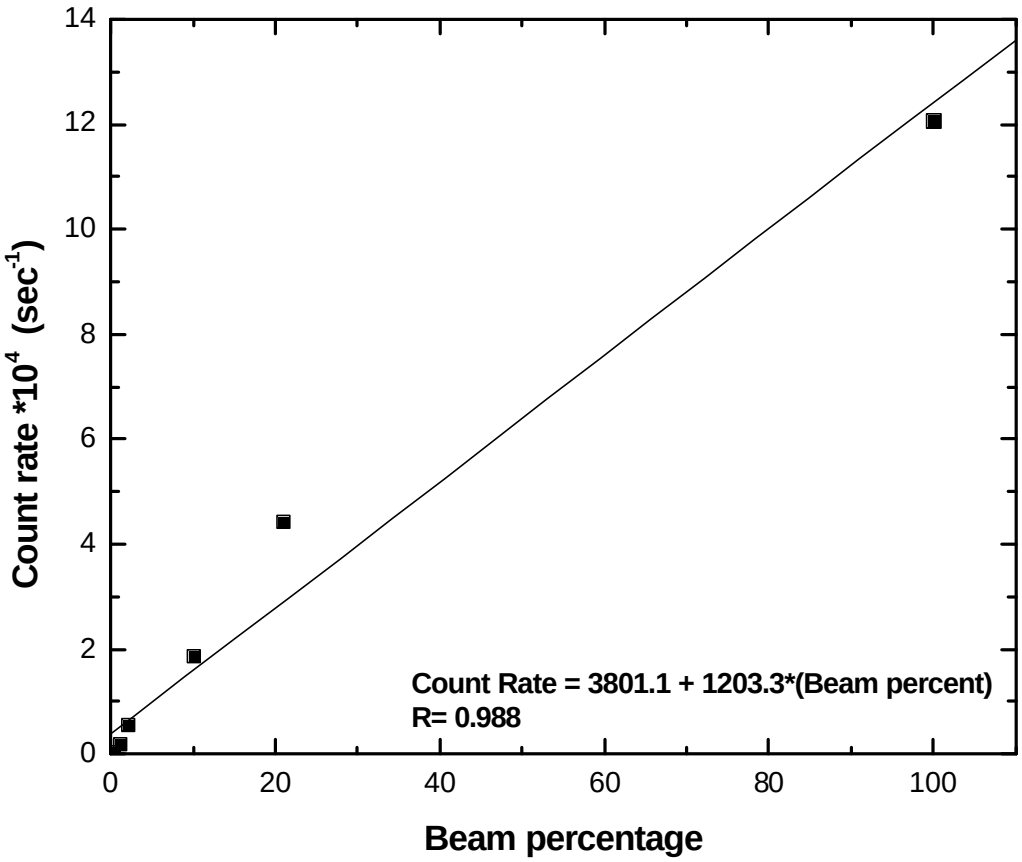


**Figure 3.12** A plot of the count rate vs. the percentage of the ion beam measured from the back channel plate of the beam veiwer. The solid line indicates the fit to the data. Parameters A, and B are the slope and y-intercept, and R is the regression fit to the data.

rate versus the beam percentage, with a linear fit to the data. The fit is not excellent, giving a large y-intercept, and a regression fit of R = 0.988. By removing the last point from the data set, and re-plotting, a much better fit to the data is achieved, as shown in **Figure 3.13**. Here, the fit is much better, and the relationship between the counts/second and the beam percentage is clearly linear. This indicates that for count

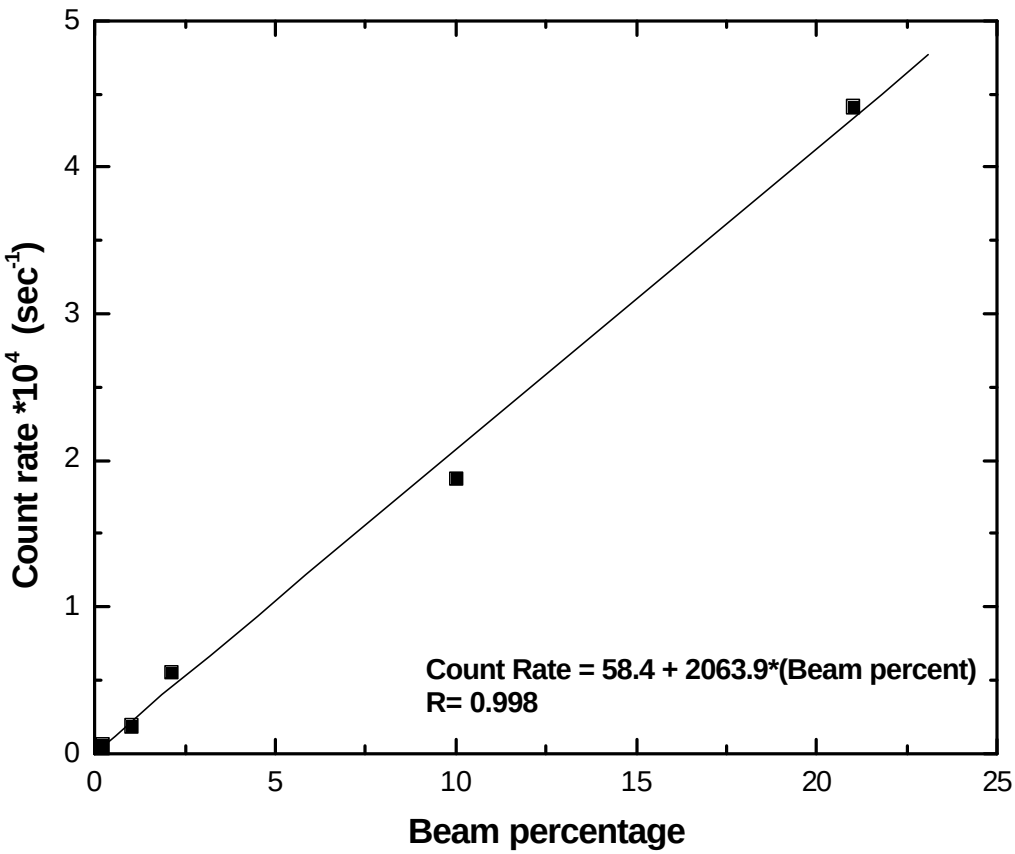


**Figure 3.13** A plot of the count rate vs. the percentage of the ion beam, and a fit to the data (with the last point removed). The fit to the data is better than in **Figure 3.12**.

rates below the level where the data deviates from linear, the counting will be reliable. From the graph in **Figure 3.13**, it can be seen that the counting is reliable for count rates at or below 45,000 counts per second.

The first pressure measurement involved scanning the target pressure (helium gas) over a wide range. The count rates of the primary, single and double capture were recorded as the pressure was scanned from 2-80 $\times 10^{-5}$ mb. The results of this pressure scan can be seen in **Figure 3.14**, where the count rates of the primary, single double-capture beams, and the total (or sum) have been plotted. The single capture beam appeared fairly linear for pressures ranging from 2-10 $\times 10^{-5}$ mb, but at higher pressures, double capture became dominant. The capture of three or more electrons was not measured, but may be likely for the data points taken at the higher pressures of this scan. When changing to different pressures, the total beam current reaching the beam viewer fluctuated. This fluctuation was partially due to small drifts in the beam current generated from the **CRYEBIS**, and also capture of several electrons resulting from multiple collisions. This first scan indicated that the region best suited for single collisions was in the range of 2-10 $\times 10^{-5}$ mb.

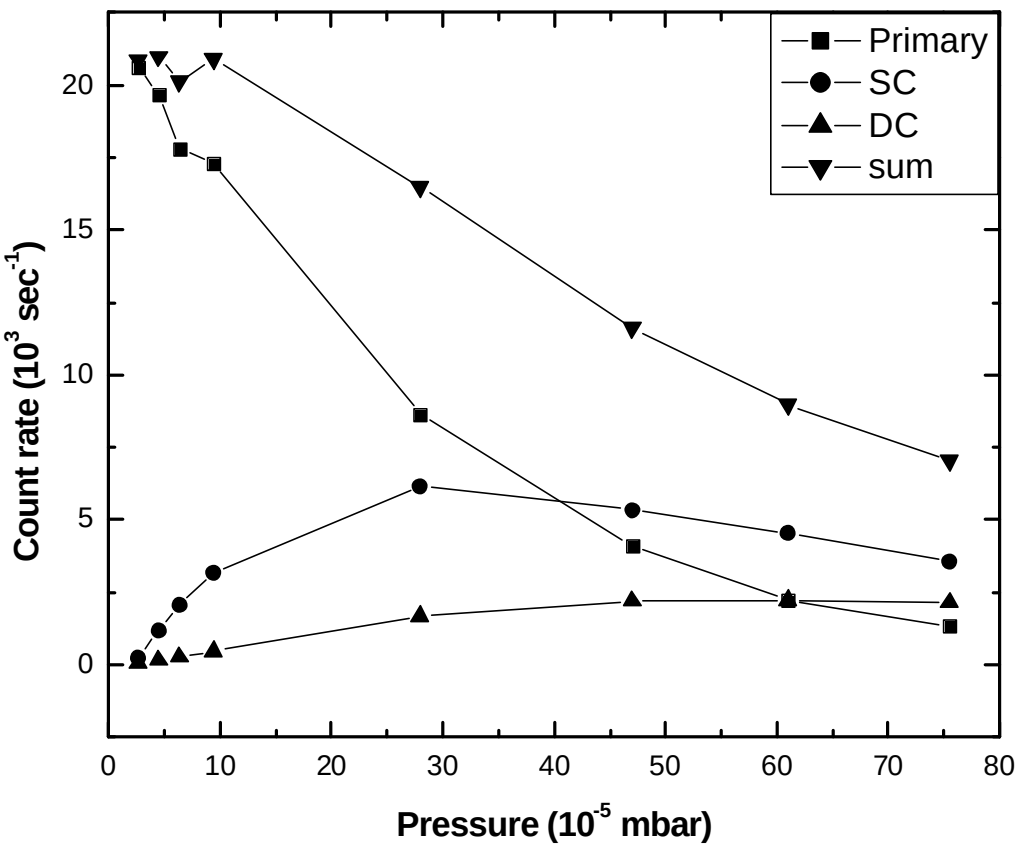


**Figure 3.14** The count rate of the primary, single, and double-capture beams, and the sum plotted as a function of the target pressure. The lines connecting the points are to guide the eye.

Concentrating on the region from 2-10 $\times 10^{-5}$ mb, another count rate versus pressure scan was taken, and the results are shown in **Figure 3.15**. The total count rate was nearly constant in the range of pressures scanned to make this plot. It was observed that the ion beam current fluctuated by a few thousand counts per second, and is likely the reason for the dip in the total count rate for the point taken at $6.8 \times 10^{-5}$ mb. Again, the lines connecting the points in **Figure 3.15** are to guide the eye.

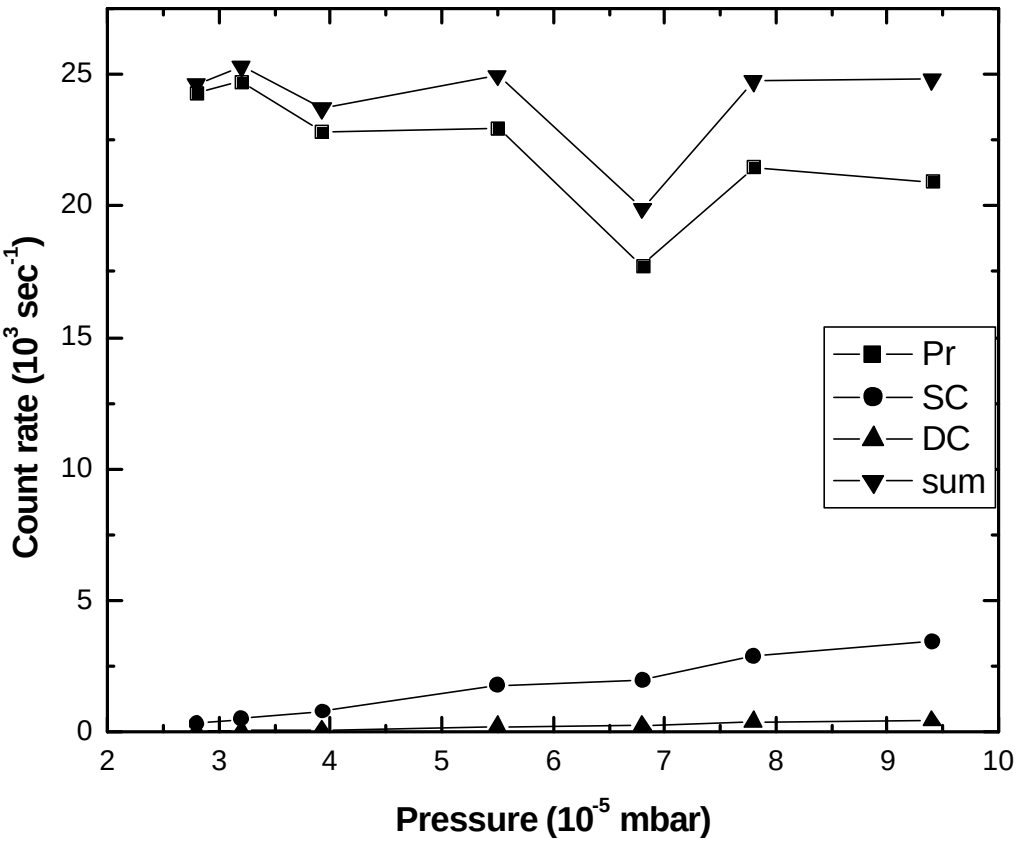


**Figure 3.15** The count rate of the primary, single, and double-capture beams, and the sum plotted as a function of the target pressure from 2 to $10 \times 10^{-5}$ mb. The lines connecting the points are to guide the eye.

Linear fits to the single capture and double capture beams have been made, and can be seen in **Figure 3.16**, and **Figure 3.17**. The fits to the data are good, and both the single capture and double capture beams exhibit linearity. In this regime, the probability of double capture, due to two collision events for the same projectile ion is approximately equal to the square of the probability for single capture. The ratio of single capture count to the total beam count is between 5-10 % for this linear relationship to exist, leading to a

contribution of double capture from double collisions of less than 1% of the single capture beam. For higher pressures, the number of double electron-capture ions will increase in a non-linear fashion since the probability that the projectile ion will capture electrons from more than one atom increases.

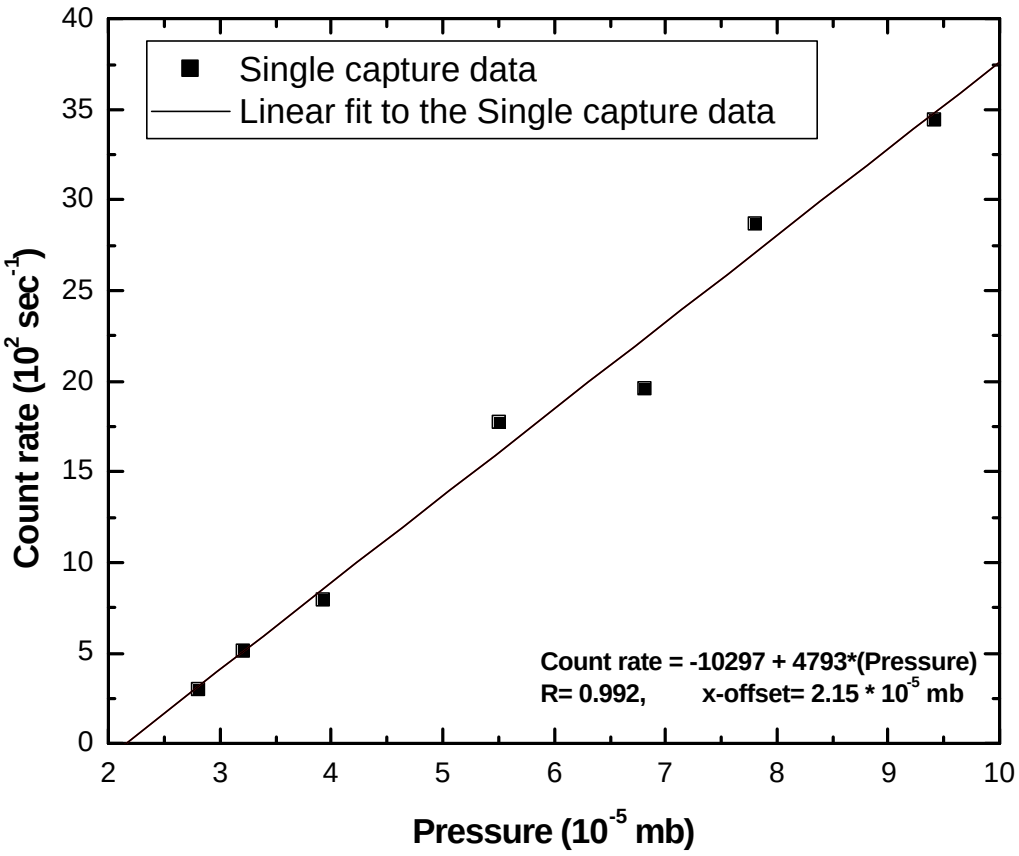


**Figure 3.16** The single capture count rate versus target pressure, and a linear fit to the data.

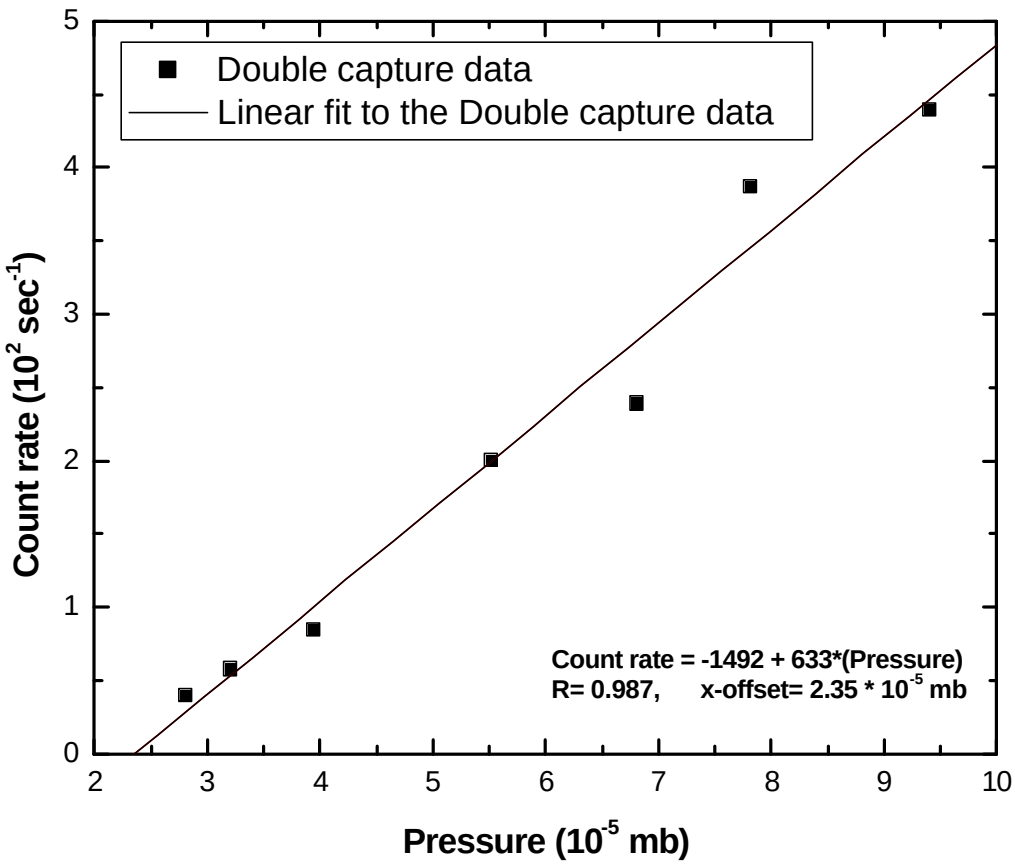


**Figure 3.17** The double capture count rate versus target pressure, and a linear fit to the data.

Approximately 1 % of the total count rate is from double capture, and about 5-15% of the total count is from single capture at a pressure around $6 \times 10^{-5}$ mb. This is a typical pressure used when taking measurements (for most targets studied). As a rule of thumb, the target pressure was adjusted until approximately 5% of the beam went into single capture. Under these operating conditions, there is no significant loss from the single capture beam, however the double capture cross section will have a considerable contribution of its count rate from double collisions, where there is two consecutive single capture events from different targets. The contribution of double capture from

double collisions can be estimated by taking the square of the single capture fraction (which is listed for each system).

From the linear fits to the data, it was observed that the y-intercept was negative. The pressures at which the count rates goes to zero are, $2.15 \times 10^{-5}$ mb, and $2.35 \times 10^{-5}$ mb, for the single and double capture beams respectively. This gives an average offset of $2.25 \times 10^{-5}$ mb. This implies that the meter used to measure the pressure reads high by this amount. The actual pressure in the gas cell is the value displayed on the meter, minus this offset, and this is the value for the pressure that is used in calculating electron capture cross sections.

## E. Detection of Charge Transfer Events

Once the series of charge states are clearly focused on the beam viewer, the beam viewer can be retracted from the beam line so that the ions will pass the beam viewer, and can be measured the position sensitive detector. As mentioned previously, it is sometimes necessary to measure the primary and single electron capture in one run, and then, repeat a second run, with all conditions being the same for the run except that the analyzing magnet is adjusted slightly so that the single electron capture and double electron capture beams are measured. The reason for measuring the primary and single capture beam in one run, and the single and double capture beam in the following run, is because of the limitations of how clearly the different charge states can be resolved. The three beam spots take up more space than can simultaneously fit on the detector. In order to separate the charge states clearly, it is necessary to take 2 separate runs. Since the ratio of the number of counts for the sum of the primary beam, single capture and double

capture, to the counts for the single capture beam, and the number of counts of the primary beam, single capture and double capture to the number of counts of the double capture beam are needed to calculate single and double electron capture cross sections, the count rate for each charge state needs to be measured individually.

A standard wedge and strip backgammon germanium detector is used to detect the position of the ions. A negative 5 kV Bertran power supply is used to set the potential on the front (upstream) MCP to negative 2 kV. The detector uses 2 micro-channel plates (MCPs), stacked in the "chevron" configuration, which generate an "avalanche" of electrons, which are expelled onto the grounded germanium anode. The electron "avalanche" is a large enough signal to be detected on the anode. The anode has electrodes connected to it for the x, y, and r surfaces of the detector. The signals that come from the x, y, and r outputs of the detector are amplified with EDL **[3.11]** preamps. The outputs of the EDL preamplifiers are used as a signal for input to Tennelec (model TC 247) amplifiers. The outputs of the amplifiers are input to an Ortec 811 analog-digital converter (ADC) mounted in a **CAMAC** crate. Also, a timing signal is derived from the back (downstream) MCP. This is input to an EG&G Ortec (VT 120) preamplifier. The output of the EG&G Ortec preamplifier is input to a Phillips Scientific quad fast rise-time amplifier (Model 774), and the output of this goes to a Tennelec TC 453 constant fraction discriminator. The output of the constant fraction discriminator is input to an Ortec gate and delay generator (Model 416A). Finally the output of the gate and delay generator is used as the strobe input on the ADC, which triggers the CAMAC LAM (look at me) flag, indicating data acquisition. This is shown schematically in **Figure 3.18**.

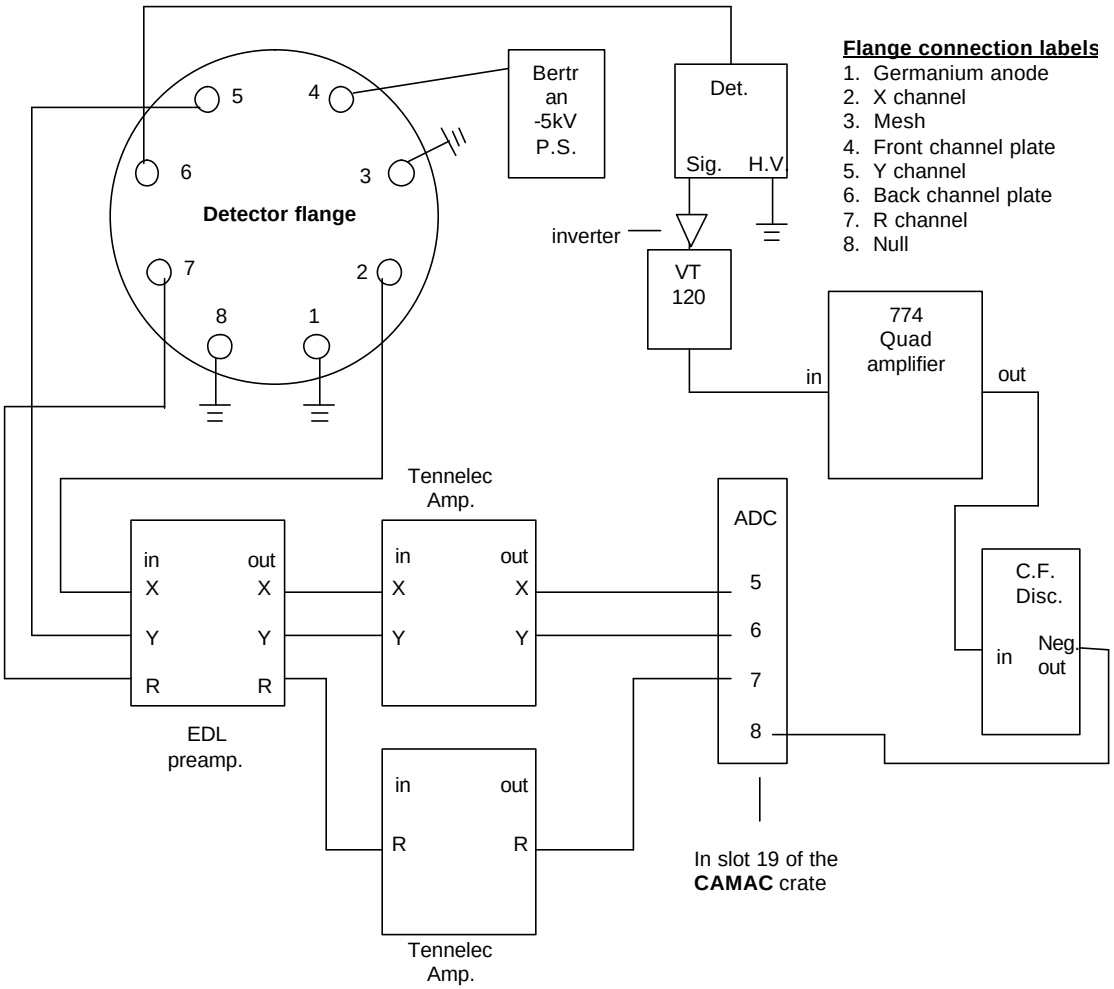


**Figure 3.18** Schematic diagram of the electronics used for the position sensitive detector.

The position of the primary beam, single capture beam, and the double capture beam can be viewed on the **CRYEBIS** Vax station using the XSYS software package **[3.12]**. One dimensional gates are set in software (see **Appendix 2** for the code used for data accumulation), and are used to set upper and lower position boundaries to determine what is counted as primary beam, single capture beam, and double capture beam. Several

spectra are displayed from the XSYS program on the Vax station, and will be explained in more detail in the next chapter.

To ensure that the detector is not saturated, and to keep "dead time" to a minimum, attenuators are used to block some fraction of the ion beam. The **CRYEBIS** was usually run with a duty cycle of approximately 10%, so the count rate on the detector was kept at or below 500 counts/sec, in order to keep the instantaneous count rate below 5000 counts/sec.

## F. Determination of Ion Beam Energies at Very Low Velocities

As a separate experiment to determine the ion beam energy and energy spread, retarding meshes were placed directly in front of the position sensitive detector, and the ion beam count rate was measured as a function of the voltage applied to the retarding meshes (without use of the **OPIG)**. As the voltage of the retarding meshes is increased up to a level where it is equal to the extraction voltage of the **CRYEBIS**, the ion beam count rate drops sharply to zero. The center of the "cut-off" was shifted to a slightly lower voltage than the extraction voltage of the **CRYEBIS**, which is attributed to the effect of the "space-charge" in the **CRYEBIS** drift tube.

In higher collision energy experiments, a difference of a few volts on a power supply may not be an important issue, but for very low collision energies, a few volts difference between one power supply and another may make a substantial difference in determination of the collision energy. In order to ensure that the potential applied to the retarding meshes was the same as applied to the **OPIG**, a reversed-biased battery box, which was capable of outputting a voltage between -240 to 0 Volts was connected in series to the extraction voltage of the **CRYEBIS**. This, then gave an output tunable

between about 1810 V and 1950 V with respect to ground, for a **CRYEBIS** extraction voltage equal to 1950 V. This battery-box was also used when making energy calibration measurements on the **OPIG**, to properly compare the "cut-off" spectra. The output of the battery box was applied to the retarding meshes, while the **OPIG** was turned off, and then a separate measurement was taken with the retarding meshes turned off, and the output of the battery box going to the **OPIG**. Also, to ensure that the ions actually passed through an electric potential equal to the value set on the retarding meshes, a very fine (333 line per inch **[3.13]**) mesh was used, and four mesh pieces were arranged as shown in **Figure 3.19**.

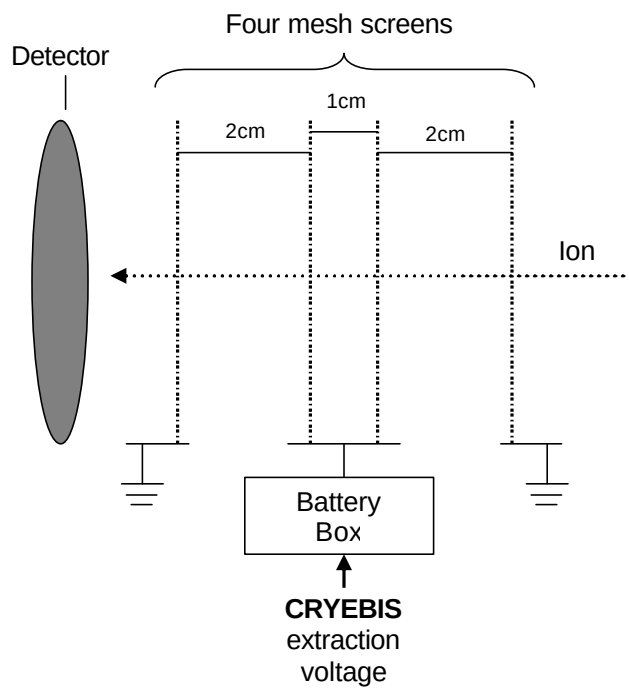


**Figure 3.19** Diagram showing the configuration of the 4 meshes used in retarding the ion beam for calibrating the energy of ions extracted from the **CRYEBIS**. As the voltage is increased (on the two inner meshes) to a voltage greater than the extraction voltage on the **CRYEBIS**, the ions will no longer have enough energy to pass through the mesh system.

An interesting artifact from the cut-off measurements taken with the **OPIG**, was the presence of a small peak, or hump in the data, just before the cut-off point. This hump was only present when the retarding meshes were situated in front of the PSD. The reason for the presence of this hump is not entirely clear, but being at a point where the collision energy is very small, it is possible that it is due to ion scattering. The presence of the hump was actually quite useful to assist in locating a point of reference to define as the onset of the cut-off. Furthermore, since the hump amplitude was observed to be independent of the projectile charge state, it "divided out" when determining cross sections.

Under normal operating conditions, the average electron beam current on the **CRYEBIS** is typically around 24-25 mA, with an extraction voltage of 1950 V. Using $N^{7+}$ as the projectile ions, the center of the "cut-off" was at 1896 V, giving a measured shift due to "space-charge" of 54 V. The electron beam current was changed to 6.7 mA, and the center of the "cut-off" shifted to 1939.2 V, supporting the hypothesis that the difference between extraction and measured cutoff voltages was due to a "space-charge" effect. This "cut-off" measurement, using the retarding meshes, not only helped in determining the extracted ion energy for the **OPIG** experiment, but has also helped characterize the **CRYEBIS** space-charge effect, which might be useful in other future experiments.

When performing the same type of "cut-off" measurement using the **OPIG** to cut the beam (in place of the retarding meshes) a similar "cut-off" spectra was observed. The center of the "cut-off" was observed at the same voltage setting as that obtained using the retarding meshes, with an error of about 1 volt. By taking a derivative of the "cut-off"

spectra and fitting the resulting peak to a Gaussian, it was found that for both the retarding mesh measurement, and the **OPIG "**cut-off" measurement, that both the full width at half the maximum heights (FWHM) were about 4 V. This width is then the energy spread ($\Delta E = \Delta Vq$) of the ions extracted from the **CRYEBIS**, and ultimately is what limits how low in collision energy meaningful experiments can be performed using the **CRYEBIS** in conjunction with the **OPIG**. The FWHM for $N^{(5\text{-}7)+}$ all had widths of about 4 volts.

**Figure 3.20a** shows a cut-off curve using the retarding meshes; **Figure 3.20b** shows the derivative of the cut-off curve. The center of the cut-off for this measurement was at a retardation potential of 1896 volts, and the energy of the beam is defined by this voltage.

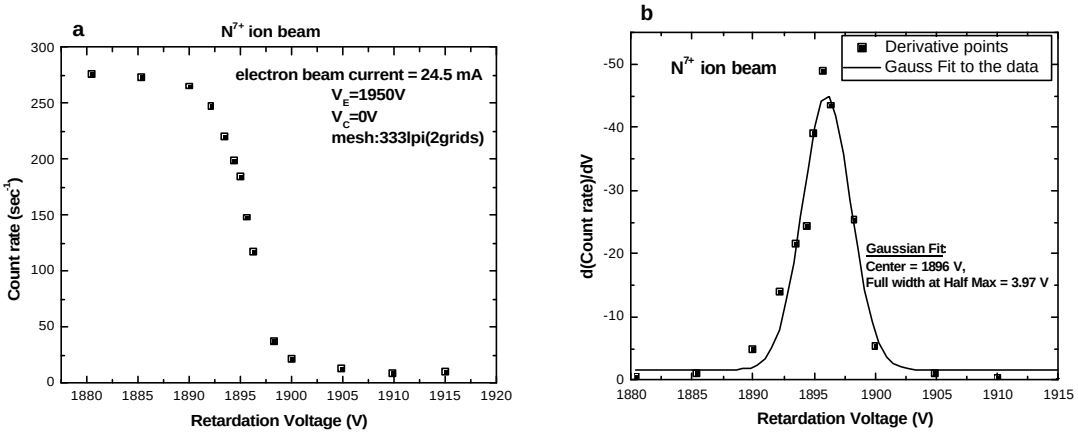


**Figure 3.20** An ion beam cut-off curve generated using a set of retarding meshes is shown in **a**. In **b**, are plotted the derivative of the data points from the curve shown in **a**. A Gaussian fit to the derivative is shown as a black line.

The collision energy in these experiments is defined with respect to the center of the cut-off. That is the center of the cut-off is defined as the voltage where the collision energy is zero. When running experiments, a high voltage power supply (Spellman, 0-5 mA, 0-10 kV) was "floated" on a lower voltage ramp generator (IKF). A typical setting for the high voltage power supply, after optimizing the tuning of the ion beam for very low energy collisions, was about 1800V (for an extraction voltage, $V_E$ = 1950V). The collision energy was typically scanned from 0 - 150eVq/amu, where the ramp generator was employed to vary the energy. The ramp generator also has an output of 0 - 8V, which corresponds linearly to the 0 – 150V ramp output. This 0 – 8V output, is reduced to a 0 – 2V signal with a voltage divider. The 0 – 2V signal is sent to the ADC, where its value is recorded for each event on the PSD. Each channel in an XSYS spectrum corresponds to a ramp voltage of 1.1719 V applied to the **OPIG**. The electron beam current on the **CRYEBIS** was set to 24.7 mA for the data points taken in **Figure 3.20** and **Figure 3.21**

In **Figure 3.21**, a cut-off curve using the **OPIG** (with the retarding meshes grounded) is shown, where all settings on the **CRYEBIS** are the same as for the curve in **Figure 3.20**, and the energy of the ion beam is identical. The center of the cut-off, is located at the same potential of 1896 volts. The potential where the ion beam has "zero" energy is essentially the same using either the retarding meshes, or the **OPIG**. This is a good thing, and demonstrates that the **OPIG** operates in accordance with its design. Only data for $N^{7+}$ is shown (to illustrate the point) but, for all other ions measured, when comparing the center of the cut-off ("zero" energy point) it was identical for the retarding meshes, and the **OPIG**.

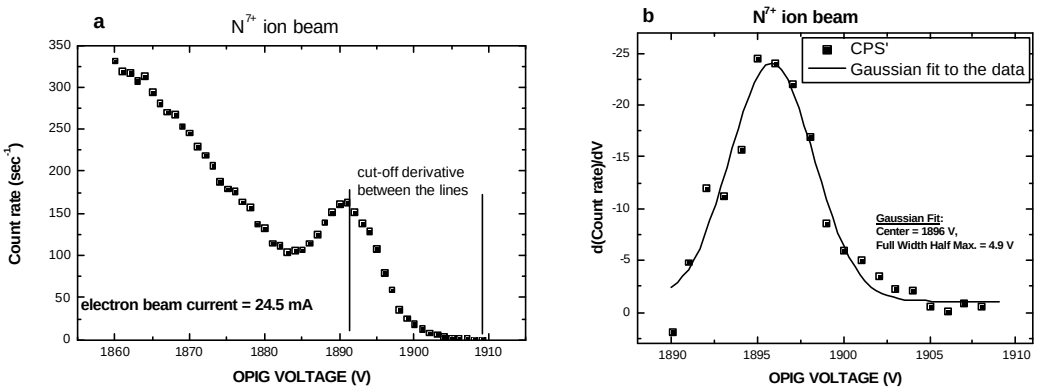


**Figure 3.21** An ion beam cut-off curve generated using the **OPIG** is shown in **a**. In **b** is shown the derivative of the data points from the curve shown in **a**. A Gaussian fit to the derivative is shown as a black line. (In **a**, the dip in the count rate near 1883 V is attributed to loss from ion beam optics on the downstream end of the **OPIG**)

Varying the electron beam current on the **CRYEBIS** changed the energy of the beam, but did not influence the energy spread of the beam. The "space-charge" effect is related to the electron beam current, and its effect can be seen as a shift in voltage of the center of the cut-off curve. For ions, $N^{5+}$, $N^{6+}$, and $N^{7+}$, cut-off curves were measured using the retarding meshes with an electron beam current of 6.7 mA. Again, the **CRYEBIS** extraction voltage was set at, $V_E = 1950V$. By comparing the retardation voltage at the center of the cut-off in **Figure 3.20b** with the center in **Figure 3.22b**, **Figure 3.23b**, and **Figure 3.24b**, a shift of about 45 volts is observed, which is due to the difference in the space-charge generated by the electron beam current of the **CRYEBIS**.

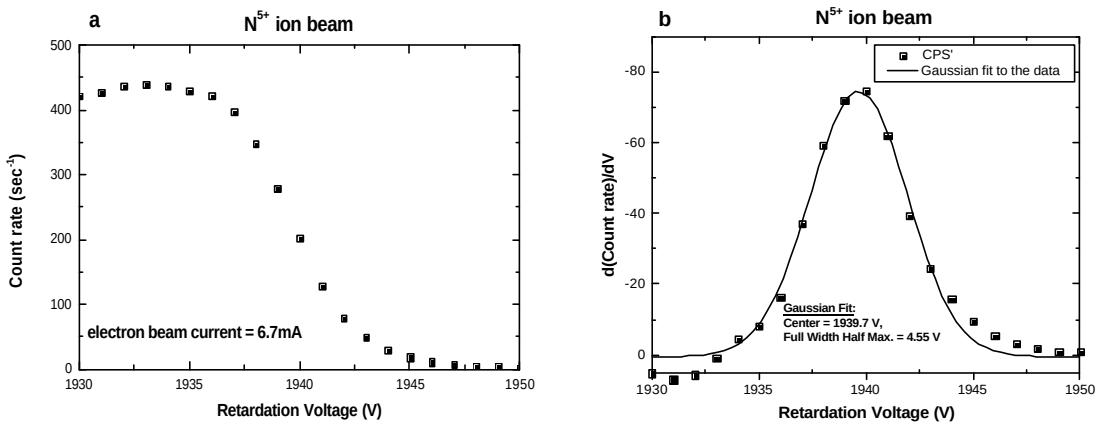


**Figure 3.22** A cut-off curve for a $N^{5+}$ ion beam, generated using the retarding meshes is shown in **a**, with the electron beam current on the **CRYEBIS** set to 6.7 mA. In **b** is shown the derivative of the cut-off curve, and a Gaussian fit to the data.

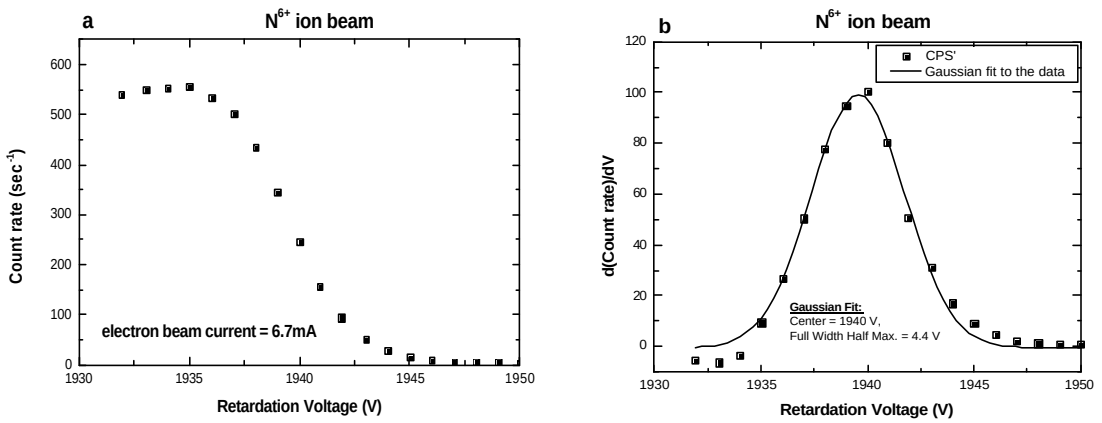


**Figure 3.23** A cut-off curve for a $N^{6+}$ ion beam, generated using the retarding meshes is shown in **a**, with the electron beam current on the **CRYEBIS** set to 6.7 mA. In **b** is shown the derivative of the cut-off curve, and a Gaussian fit to the data.

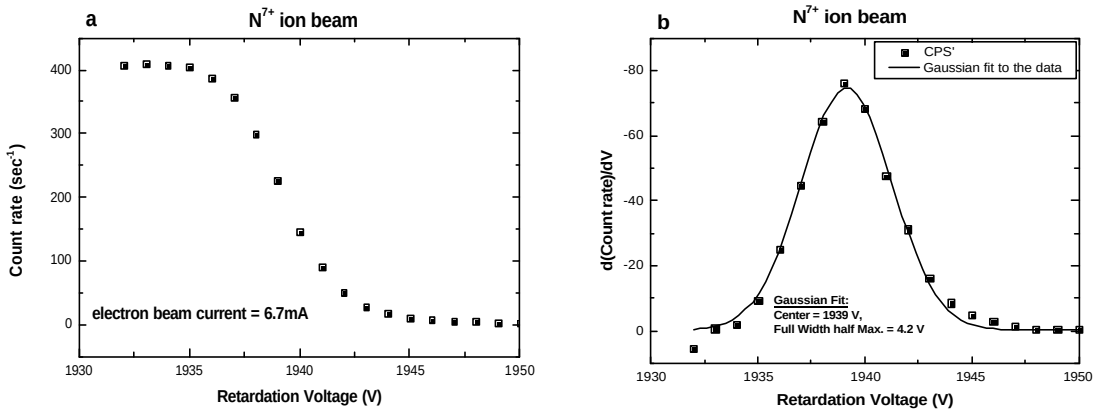


**Figure 3.24** A cut-off curve for a $N^{7+}$ ion beam, generated using the retarding meshes is shown in **a**, with the electron beam current on the **CRYEBIS** set to 6.7 mA. In **b** is shown the derivative of the cut-off curve, and a Gaussian fit to the data.